Chapter 18

Post Dryout Heat Transfer

Summary: The heat transfer process and prediction methods for describing heat transfer in the post dryout regime are presented in this chapter. First, the processes leading to the transition to the post dryout regime are described and then non-equilibrium effects. This is followed by a presentation of the leading correlations for predicting heat transfer coefficients in the post dryout regime in first vertical channels and then horizontal channels. Finally, a general method for predicting the critical heat flux in uniformly vertical tubes is presented.

18.1 Introduction

The regime of post dryout heat transfer is encountered when the heated wall becomes dry before complete evaporation. For instance, this regime is reached when an evaporating annular film dries out and the remaining liquid is entrained as droplets, such that the vapor quality x is large but less than 1.0. It also refers to heat transfer downstream from the point at which the critical heat flux has been reached, thus even when x is small or close to 0.0, or in fact when the remaining liquid in the flow is still subcooled. Post dryout heat transfer is sometimes referred to as the liquid deficient regime or as mist flow heat transfer, but these last two terms are too restrictive since they do not describe the process when it occurs at low vapor quality.

In general, the post dryout heat transfer regime is reached from the wet wall regime by passing through one of three different transitions in the evaporation process:

- *Critical heat flux*. The heat flux at the wall or the imposed wall superheat is so high that a continuous vapor film is formed on the wall, somewhat analogous to surpassing the peak nucleate heat flux in pool boiling (this is determined using a method to calculate the value of q_{crit});
- *Dryout of the liquid film*. The liquid within an annular film may completely evaporate, leaving the entrained liquid droplets in the vapor to still be evaporated (this is determined using a method to calculate the vapor quality at which dryout occurs);
- *Entrainment of the liquid film*. At some point, the vapor shear stress on the liquid film is strong enough to completely remove the film from the channel wall, such that all the liquid is entrained in the vapor phase as droplets (this is a hydrodynamic problem and can be estimated using an appropriate two-phase flow pattern map).
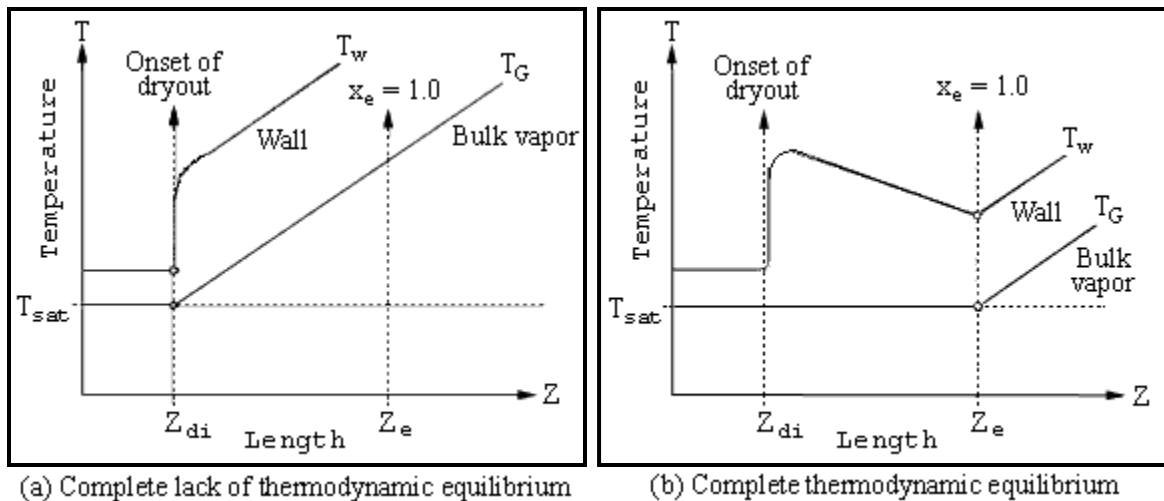
In the post dryout heat transfer regime, also often referred to as mist flow, the wall is not necessarily always dry. Entrained liquid droplets can impinge on the wall and momentarily wet it locally before either evaporating or "bouncing off" back into the vapor phase. Furthermore, only a portion of the heated periphery of the flow channel may be dry, particularly in horizontal flows and in channels with a wide variation in the peripheral heat flux (such as those heated radiantly by combustion). In particular, a progressive dryout in horizontal tubes tends to occur along the tube instead of occurring "simultaneously" around the entire perimeter as typically imagined in vertical tubes. Since the annular film is thinner at the top of the tube compared to the bottom in horizontal tubes, dryout tends to occur first at the top and then progress around the perimeter towards the bottom, creating a dryout zone along the tube.

Typically heat transfer coefficients in the post dryout regime are significantly lower than those encountered in the wet wall regime, as small as $1/10^{th}$ to $1/30^{th}$ those of the annular regime that typically

precedes it. This not only affects heat exchanger surface area calculations (e.g. most refrigeration heat exchanger design softwares do not utilize a mist flow threshold criteria and unwittingly continue modeling heat transfer as an annular flow rather than a mist flow) but perhaps the integrity of the heat exchanger itself, if the wall temperature becomes too high. The post dryout heat transfer regime may be encountered in fossil fuel boilers of electric power plants, on nuclear power plant fuel rod assemblies during a hypothetical loss of coolant, in fired heaters of petrochemical plants, and in direct-expansion evaporators and air-conditioning coils. It may also, unexpectedly, occur in liquid-liquid heat exchangers if there is a large temperature difference between the two fluids and the resulting wall temperature is significantly higher than the saturation temperature of the cold fluid.

18.2 Departure from Thermodynamic Equilibrium

During wet wall evaporation, the wall temperature remains close to the local saturation temperature corresponding to the local pressure. In contrast, in the post dryout regime, the local wall temperature may become significantly higher than the saturation temperature and hence departure from equilibrium occurs. The two limiting cases are illustrated in Figure 18.1.

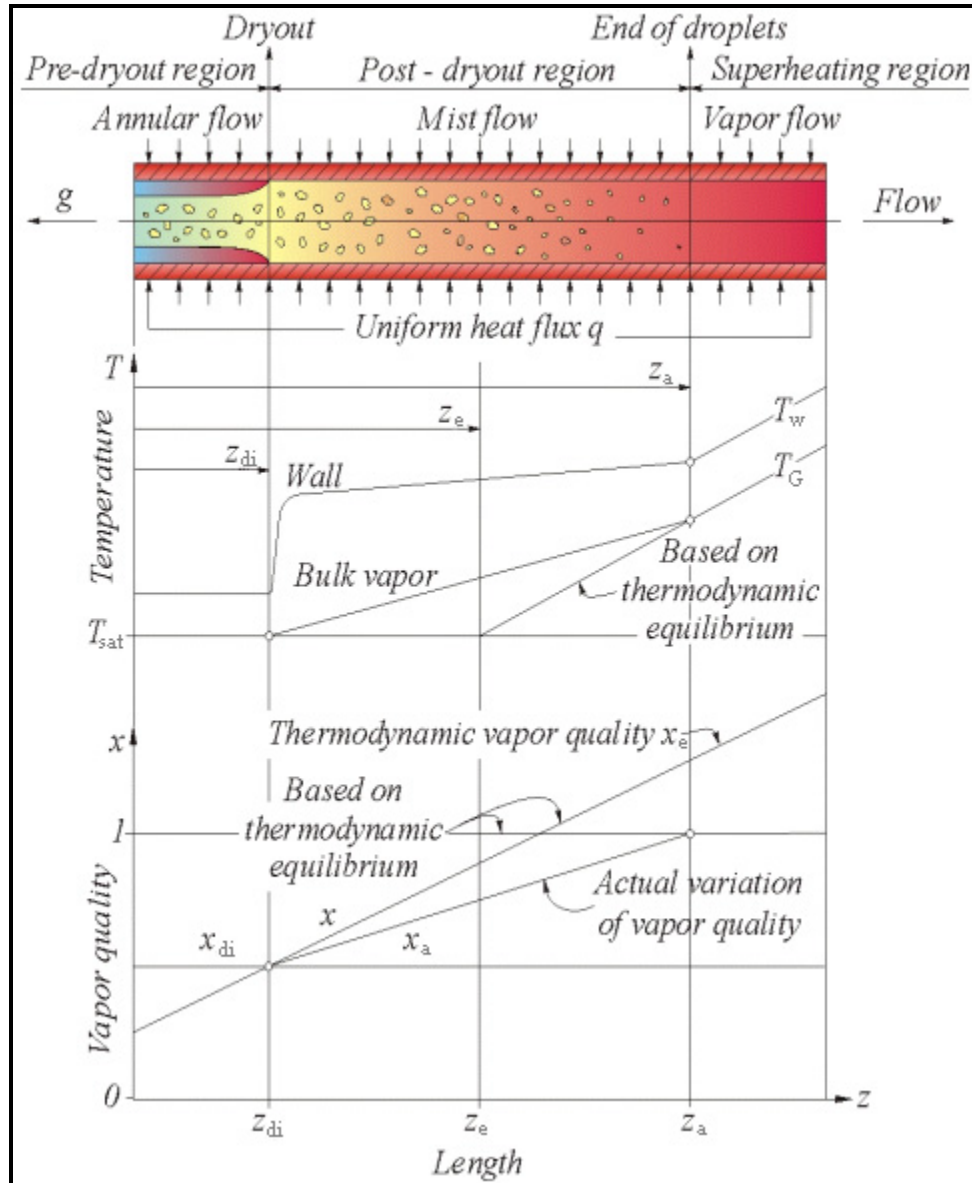(a) Complete lack of thermodynamic equilibrium   (b) Complete thermodynamic equilibrium

Figure 18.1. Thermodynamic states in the post dryout regime.

The first case represents complete departure from equilibrium, where heat is transferred only to the continuous vapor phase that is in contact with the heated wall, which results in superheating of the vapor. If the rate of heat transfer from the superheated vapor phase to the entrained droplets is so slow that their presence may be ignored, at the location z the vapor temperature $T_G(z)$ downstream of the dryout point may be calculated on the basis that all the heat added to the fluid superheats the vapor. In this case, the wall temperature $T_W(z)$ rises like that of a single-phase flow and its value can be calculated using a single-phase heat transfer correlation together with the imposed heat flux, giving the profile illustrated in Figure 18.1a.

The other limiting case is complete thermodynamic equilibrium as shown in Figure 18.1b. In this case, the rate of heat transfer from the vapor phase to the entrained droplets is assumed to be so effective that the vapor temperature $T_G(z)$ remains at the saturation temperature until all the droplets have been completely evaporated. The downstream wall temperature $T_W(z)$ may vary nonlinearly and a maximum may be reached, in part because of the cooling effect of impingement of liquid droplets on the heated wall.

The post dryout heat transfer process tends towards the case of thermal non-equilibrium, as shown in Figure 18.1a, at low pressures and low mass flow rates. At the other extreme, the process tends towards thermal equilibrium, as depicted in Figure 18.1b, at high reduced pressures and very high mass flow rates. A typical thermodynamic path of the process is illustrated in Figure 18.2 where the local temperature is lower than the maximum occurring during complete non-equilibrium, but is still significantly above the local saturation temperature of the complete equilibrium case. Hence, in post dryout heat transfer the local bulk temperature of the vapor is unknown *a priori* and thus becomes an added complication in describing and modeling the process.

Figure 18.2. Departure from thermodynamic equilibrium in the post dryout regime in a *vertical* tube.

Another complicating aspect of post dryout heat transfer is that of the local vapor quality. Thermodynamic equilibrium of the two-phases as in Figure 18.1b means that all the heat absorbed by the

fluid is utilized to evaporate the liquid and hence the local equilibrium vapor quality at location z is $x_e(z)$. On the other hand, if all the heat is used to superheat the vapor after the onset of dryout as in Figure 18.1a, the vapor quality remains fixed at that at the dryout point, $x_{di}(z)$. In reality, the actual local vapor quality $x_a(z)$ is less than that estimated from complete thermodynamic equilibrium and hence it follows that $x_{di}(z) < x_a(z) < x_e(z)$.

Consider Figure 18.2 which depicts post dryout in a *vertical* tube of internal diameter d_i heated uniformly with a heat flux of q. Dryout occurs at a length z_{di} from the inlet, and it is assumed that thermodynamic equilibrium exists at the dryout point. If complete equilibrium is maintained after dryout, all the liquid will be evaporated when the point z_e is reached. However, in the actual situation, only a fraction (κ) of the surface heat flux is used to evaporate the remaining liquid in the post dryout region, while the remainder is used to superheat the bulk vapor. The liquid is thus completely evaporated only when a downstream distance of z_a is reached.

Now, assume that q, the total heat flux from the tube wall to the fluid at location z, can be subdivided into two components: the heat flux associated with droplet evaporation $q_L(z)$ at location z and the heat flux associated with vapor superheating $q_G(z)$ at location z. Thus,

$$q = q_L(z) + q_G(z)$$ [18.2.1]

Furthermore, let

$$\kappa = q_L(z)/q(z)$$ [18.2.2]

For simplicity, κ is considered independent of the length along the tube z, although this is not the case in general. Hence, the profiles of the actual bulk vapor temperature and actual vapor quality are linear as shown in Figure 18.2. The variation in the thermodynamic vapor quality with tube length for $z < z_e$ is given by an energy balance

$$x(z) - x_{di} = \frac{4q}{d_i \dot{m} h_{LG}} (z - z_{di})$$ [18.2.3]

where h_{LG} is the latent heat of vaporization and $\dot{m}$ is the total mass velocity. The location of point z_e is given by

$$z_e = \left[\frac{d_i \dot{m} h_{LG}}{4q} (1 - x_{di}) \right] + z_{di}$$ [18.2.4]

The actual vapor quality $x_a(z)$ variation with length for $z < z_a$ is given by

$$x_a(z) - x_{di} = \frac{4\kappa q}{d_i \dot{m} h_{LG}} (z - z_{di})$$ [18.2.5]

and z_a is given by

$$z_a = \left[\frac{d_i \dot{m} h_{LG}}{4\kappa q}(1 - x_{di})\right] + z_{di} \qquad [18.2.6]$$

By combining [18.2.3] and [18.2.6], the resulting expression for κ is

$$\kappa = \left[\frac{x_a(z) - x_{di}}{x(z) - x_{di}}\right] = \left[\frac{z_a - z_{di}}{z_e - z_{di}}\right] \qquad [18.2.7]$$

Similarly, the actual bulk vapor temperature $T_{G,a}(z)$ is obtained:

$$T_G(z) = T_{sat} + \left[\frac{4(1 - \kappa)q(z - z_{di})}{\dot{m} c_{pG} d_i}\right] \qquad [18.2.8]$$

for $z < z_a$ while for $z_a > z$ it is:

$$T_G(z) = T_{sat} + \left[\frac{4q(z - z_e)}{\dot{m} c_{pG} d_i}\right] \qquad [18.2.9]$$

The two limiting cases illustrated in Figure 18.1 are clearly recognized by setting $\kappa = 0$ and $\kappa = 1$, respectively, in the above expressions. In reality, κ is not independent of tube length and must be predicted from the actual process conditions.

From a practical standpoint, as shown in Figure 18.2, liquid may remain entrained as small droplets in the vapor well beyond the location of $x_e(z)$. This fine mist gives rise to thermodynamic non-equilibrium and affects the thermal efficiency of a vapor compression or power cycle. For processes requiring dry saturated vapor or dry superheated vapor, such as a compressor or steam turbine, wet vapor can represent an operational liability.

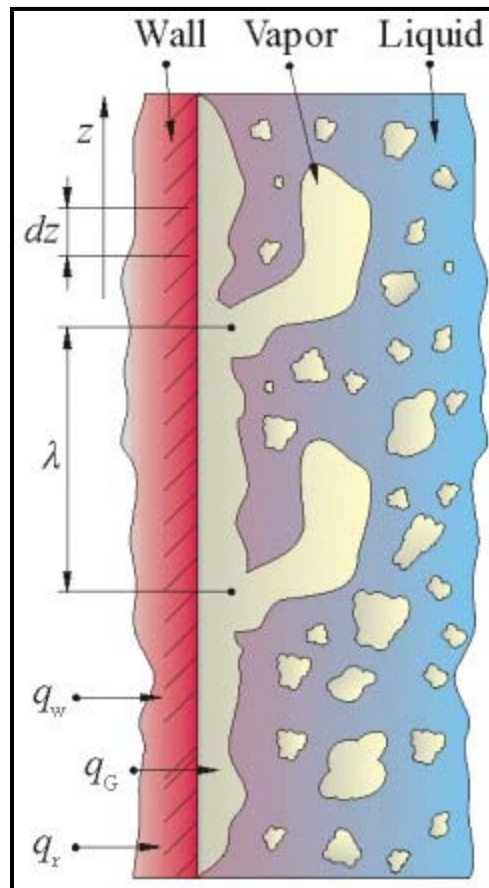## 18.3 Heat Transfer Regimes and Mechanisms

Two principal types of evaporation processes are encountered in the post dryout heat transfer regime. The first of these is the *dispersed flow regime*, in which the vapor phase becomes the continuous phase and all the liquid is entrained as dispersed droplets as illustrated in Figure 18.2. The second process is that of *inverted annular flow*, in which the vapor forms an annular film on the tube wall and the liquid is in the central core as shown in Figure 18.3 (where q_w is the wall heat flux, q_r is the radiant heat flux from the wall to the liquid and q_G is the heat flux across the vapor film to the interface while λ is the wavelength between bubble departures from the interface). The dispersed flow regime typically occurs after dryout or entrainment of an annular film flow. The inverted annular flow regime is encountered when the critical heat flux is surpassed for a flow at low vapor quality or even for subcooled liquid. In this case, the wall is too hot to be rewetted by the liquid and a continuous but highly disturbed vapor film is formed between the wall and the continuous liquid core.

For horizontal and inclined tubes, where dryout does not occur uniformly on the tube perimeter, only the upper part of the tube wall may be in the post dryout heat transfer regime while the lower part remains wet. This may also occur in vertical or inclined tubes that are heated non-uniformly, e.g. in the radiant

section of a fired heater or fossil fuel steam generator, where only one side of the tube is exposed to the flame.

Before discussing methods for predicting post dryout heat transfer coefficients in the next sections, it is instructive to first look at possible modes of heat transfer under these conditions:

- *Wall-to-vapor heat transfer*. Heat is transferred by convection from the wall to the continuous vapor phase in the dispersed flow regime (similar to single-phase flow in a channel) while in inverted annular flow heat is transferred by conduction (or convection) across the vapor film to the interface of the liquid core;
- *Wall-to-droplet heat transfer*. Heat is transferred to the droplets that impinge on the hot wall, which may be completely evaporated or only partially so before becoming re-entrained. The impinging droplets are evaporated either by transient, thin film evaporation or by nucleate boiling within the film if sites become active when a large droplet impacts on the wall;
- *Vapor-to-droplet heat transfer*. Heat is transferred by convection from the bulk-superheated vapor to the saturated liquid in the droplets. The saturation temperature is a function of the radius of the droplet (analogous to a bubble nucleus) and makes complete evaporation difficult to attain as the radius becomes small and smaller. Heat is also transferred by convection to any droplets passing through the thermal boundary layer on the wall that do not actually contact the wall;

Figure 18.3. Inverted annular flow regime.

- *Radiation heat transfer from the wall-to-droplets/vapor/upstream wall*. This mechanism only becomes important at large superheats. The vapor is almost transparent to thermal radiation while the droplets tend to absorb, transmit and reflect radiation and thus evaporate. The downstream wall also exchanges radiant energy with a hotter or cooler upstream wall. The net radiation flux depends on the view factor, the emissive properties of the surface and the respective temperatures.

18.4 Heat Transfer in Inverted Annular Flow

This regime is illustrated in Figure 18.3 and is also sometimes referred to as forced convection film boiling. Dougall and Rohsenow (1963) made observations of film boiling inside a vertical tube and they noted that at low vapor quality and low flow rates the flow structure consisted of a central liquid core and a thin annular film of vapor on the heated wall. The interface between the two phases was not smooth but noticeably disturbed by waves traveling at a velocity similar to that of the liquid core. Because of the density difference between the two phases, the vapor was assumed to be traveling at a much higher velocity than the liquid core. Depending on the imposed conditions on vertical upward flow, the liquid core was observed to flow upward, remain more or less stationary, or even flow downward. Entrained vapor bubbles were also observed in the liquid core.

Inverted annular flow heat transfer is particularly amicable to analytical analysis because the problem of bubble nucleation at the heated wall is not present. In fact, the heat transfer through the vapor film can be treated as an analogy to film-wise condensation. Solutions are available for a variety of heated surface geometries for internal and external flows for both laminar and turbulent conditions with and without interfacial stress. The simplest situation is that of a laminar vapor film with a linear temperature profile. For a vertical flat surface, the analysis is similar to the Nusselt solution for falling film condensation on a vertical flat plate, and the local heat transfer coefficient α_{invert} at a distance z from the point of onset of film boiling is

$$\alpha_{invert} = C\left[\frac{k_G^3 \rho_G (\rho_L - \rho_G) g h_{LG}}{z \mu_G \Delta T}\right]^{1/4} \qquad [18.4.1]$$

In this expression, the wall superheat is $\Delta T = (T_w - T_{sat})$. The value of the constant C depends on the boundary conditions. For zero interfacial stress $C = 0.707$ while for zero interfacial velocity $C = 0.5$.

Wallis and Collier (1968) also analyzed inverted annular flow with a turbulent vapor film. They arrived at the following expression in which the heat transfer coefficient is inversely dependent on the distance z:

$$\frac{\alpha_{invert} z}{k_G} = 0.056 \, Re_G^{0.2} \left[Pr_G \, Gr_G\right]^{1/3} \qquad [18.4.2]$$

Pr_G is the vapor Prandtl number while Gr_G is the vapor Grashof number, defined as

$$Gr_G = \frac{z^3 g \rho_G (\rho_L - \rho_G)}{\mu_G^2} \qquad [18.4.3]$$

The vapor Reynolds number Re_G is that of the vapor fraction flowing alone in the tube, i.e. the vapor flow is assumed to occupy the total cross-section of the tube, which is also sometimes referred to as the vapor only Reynolds number and given the symbol Re_{Go}. This expression is similar to the empirical expressions for turbulent, falling film condensation. More complex analytical approaches attempt to capture important aspects of the flow structure at the interface, such as waves, periodic disturbances, instabilities, subcooling of the vapor core, etc.

Example 18.1: Determine the local heat transfer coefficient for inverted annular flow at distances of 0.01, 0.1, 0.5 and 1.0 m from the lower edge of a vertical plate heated to a uniform temperature of 150°C. The fluid has the following physical properties at its saturation temperature of 100°C: liquid density is 1200 kg/m³, vapor density is 20 kg/m³, vapor thermal conductivity is 0.01 W/mK, latent heat of vaporization is 200 kJ/kg and vapor viscosity is 0.000011 Ns/m².

Solution: Substituting the values into [18.4.1] and assuming no interfacial stress (so $C = 0.707$) gives:

$$\alpha_{invert} = 0.707\left[\frac{(0.01)^3 (20)(1200 - 20)(9.81)(200000)}{z(0.000011)(150 - 100)}\right]^{1/4} = \frac{67.72}{z^{1/4}}$$

Thus, the local heat transfer coefficients at 0.01, 0.1, 0.5 and 1.0 m are 214.2, 120.4, 80.5 and 67.7 W/m^2K, respectively. Thus, the local heat transfer coefficient decreases as z increases and the local heat flux, i.e. $q = \alpha_{invert} \Delta T$, ranges from 10710 to 3386 W/m^2.

18.5 Heat Transfer in Mist Flow in Vertical Channels

Numerous empirical methods for predicting heat transfer in the mist flow regime, i.e. the dispersed liquid regime, have been proposed, in vertical tubes. Most can be classified as simple modifications of single-phase heat transfer correlations such as that of Dittus-Boelter (1930). Only a representative sample of these will be presented here and more complete treatments can be found in Groeneveld (1973), Mayinger and Langer (1978) and Collier (1982). The equilibrium vapor quality is used in most of the following methods and will be referred to as x.

18.5.1. Dougall and Rohsenow Method

For single-phase turbulent flow, it is usual to use the Dittus and Boelter (1930) correlation

$$Nu = a\, Re^b\, Pr^c \qquad\qquad [18.5.1]$$

where a = 0.023, b = 0.8 and c = 0.4. The mean velocity of the fluid can be interpreted as the homogeneous velocity of the two-phases u_H:

$$u_H = \frac{\dot{m}}{\rho_H} = \dot{m}\left(\frac{x}{\rho_G} + \frac{1-x}{\rho_L}\right) \qquad\qquad [18.5.2]$$

The definition of the homogeneous vapor Reynolds number is thus

$$Re_{GH} = \frac{\dot{m}d_i}{\mu_G}\left[x + \frac{\rho_G}{\rho_L}\left(1-x\right)\right] \qquad\qquad [18.5.3]$$

Hence, assuming homogeneous flow, the mist flow heat transfer coefficient is:

$$Nu_G = \frac{\alpha d_i}{k_G} = 0.023\, Re_{GH}^{0.8}\, Pr_G^{0.4} \qquad\qquad [18.5.4]$$

This was first proposed by Dougall and Rohsenow (1963). The vapor quality to use in the expression is the equilibrium vapor quality x_e and all properties are evaluated at the saturation temperature. A similar result can be obtained making the same modification to the well-known Gnielinski (1976) correlation that covers the transition and turbulent flow regimes such that

$$Nu_G = \frac{(f/2)(Re_{GH}-1000)Pr_G}{1+12.7(f/2)^{1/2}\left(Pr_G^{2/3}-1\right)} \qquad\qquad [18.5.5]$$

where the friction factor f is obtained from

$$f = \left(1.58 \ln \mathrm{Re}_{GH} - 3.28\right)^{-2} \tag{18.5.6}$$

and Re_{GH} is defined as in [18.5.3] above.

The limitations of this type of approach are:

- All other heat transfer mechanisms in mist flow, except for wall-to-vapor heat transfer, are ignored;
- The non-equilibrium effects of superheating the vapor driving the convection process is neglected;
- The heat transfer coefficient is predicted to rise in the mist flow regime with increasing vapor quality, which is not typically observed experimentally.

Hence, this very simplified approach should only be used as a first approximation.

18.5.2 Groeneveld Method

In the above homogeneous approach, the definition of the Reynolds number is not actually consistent with homogeneous flow theory because some gas phase properties are used in conjunction with the homogeneous density when only homogeneous properties should be used. In view of this fact, Groeneveld (1973) added another multiplying factor Y defined as

$$Y = 1 - 0.1 \left[\left(\frac{\rho_L}{\rho_G} - 1 \right)(1 - x) \right]^{0.4} \tag{18.5.7}$$

to corrrect for this. The new expression for the Nusselt number is then

$$Nu_G = a \left\{ \frac{\dot{m} d_i}{\mu_G} \left[x + \frac{\rho_G}{\rho_L}(1 - x) \right] \right\}^b Pr_G^c \, Y^d \tag{18.5.8}$$

The empirical constants giving the best fit to his database are as follows: a=0.00327, b=0.901, c=1.32 and d=-1.50. The most significant change is to the exponent on the Prandtl number. The database covers the following range of conditions:

- 2.5 mm < d_i < 25 mm,
- 34 bar < p < 215 bar,
- 700 kg/m^{2}s < $\dot{m}$ < 5300 kg/m^{2}s,
- < x < 0.9,
- 120 kW/m^2 < q < 2100 kW/m^2.

This correlation is applicable to vertical and horizontal tubes and to vertical annuli. The large values of the pressure, heat flux and mass velocity in the database are typical of power boilers but they are beyond those of most other industrial applications.

Example 18.2: Compare the local heat transfer coefficients for mist flow obtained with Dougall and Rohsenow method and the Groeneveld correlation at a vapor quality of 0.85 for a tube of 22 mm diameter and a flow rate of 0.3 kg/s. The fluid has the following physical properties: liquid density is 900 kg/m^3,

vapor density is 70 kg/m^3, vapor thermal conductivity is 0.02 W/mK, vapor specific heat of 2.5 kJ/kgK and vapor viscosity is 0.000015 Ns/m^2.

Solution: First of all, the mass velocity is determined to be 789.2 kg/m^{2}s. Then, the vapor Prandtl number is calculated:

$$Pr_G = \frac{\mu_G c_{pG}}{k_G} = \frac{(0.000015)(2500)}{0.02} = 1.875$$

The vapor Reynolds number is then obtained with [18.5.3]:

$$Re_{GH} = \left(\frac{789.2(0.022)}{0.000015}\right)\left(0.85 + \frac{70}{900}(1 - 0.85)\right) = 997373$$

The Dougall and Rohsenow method is evaluated by substituting the values in [18.5.4]:

$$\frac{\alpha(0.022)}{0.02} = 0.023(997373)^{0.8}(1.875)^{0.4}$$

$$\alpha = 1693 \, W/m^2K$$

The Groeneveld correlation is evaluated by first determining the factor Y with [18.5.7]:

$$Y = 1 - 0.1\left[\left(\frac{900}{70} - 1\right)(1 - 0.85)\right]^{0.4} = 0.8741$$

The Nusselt number is obtained then with [18.5.8]:

$$Nu_G = \frac{\alpha(0.022)}{0.02} = 0.00327\left\{\left(\frac{789.2(0.022)}{0.000015}\right)\left[0.85 + \frac{70}{900}(1 - 0.85)\right]\right\}^{0.901}(1.875)^{1.32}(0.8741)^{-1.50}$$

$$\alpha = 2119 \, W/m^2K$$

Thus, the Groeneveld correlation gives a heat transfer coefficient 25% larger than the Dougall and Rohsenow method.

18.5.3 Groeneveld and Delorme Method

Groeneveld and Delorme (1976) subsequently proposed a new correlation that empirically accounts for the non-equilibrium effects. The new correlation has the same form as Groeneveld's earlier expression but with one additional empirical group. Notably, the actual non-equilibrium temperature $T_{G,a}$ and actual vapor quality x_a are utilized rather than the saturation temperature and equilibrium vapor quality. The new expression is

$$\frac{\alpha d_i}{k_{G,f}} = \frac{q d_i}{(T_w - T_{G,a})k_{G,f}} = a\left[\left(\frac{\dot{m} d_i}{\mu_{G,f}}\right)\left(x_a + \frac{\rho_G}{\rho_L}(1 - x_a)\right)\right]^b Pr_{G,f}^c\left(e + f\frac{d_i}{L}\right)^g \qquad [18.5.9]$$

Although the above expression may be used with its numerous empirical constants (refer to their publication), Groeneveld and Delorme found that using the following simpler expression also predicted their data quite well:

$$\frac{\alpha d_i}{k_{G,f}} = \frac{q d_i}{\left(T_w - T_{G,a}\right)k_{G,f}} = 0.008348 \left[\left(\frac{\dot{m} d_i}{\mu_{G,f}}\right)\left(x_a + \frac{\rho_G}{\rho_L}\left(1 - x_a\right)\right)\right]^{0.8774} Pr_{G,f}^{0.6112} \qquad [18.5.10]$$

The subscript *G,f* in these expressions indicates that the vapor properties should be evaluated at the film temperature defined as

$$T_{G,f} = \left(T_w + T_{G,a}\right)/2 \qquad [18.5.11]$$

To determine the values of $T_{G,a}$ and x_a, an energy balance is used where $h_{G,a}$ is the actual vapor enthalpy and $h_{L,sat}$ is the enthalpy of the saturated liquid while x_e is the equilibrium vapor quality and h_{LG} is the latent heat of evaporation. The actual vapor quality is obtained from

$$x_a = \frac{h_{LG} x_e}{h_{G,a} - h_{L,sat}} \qquad [18.5.12]$$

The change in enthalpy is computed from the expression

$$h_{G,a} - h_{L,sat} = h_{LG} + \int_{T_{sat}}^{T_{G,a}} c_{pG} dT_G \qquad [18.5.13]$$

The approximate homogeneous Reynolds number $Re_{GH,e}$ is used, based on the equilibrium vapor quality, as follows:

$$Re_{GH,e} = \left(\frac{\dot{m} d_i}{\mu_G}\right)\left(x_e + \frac{\rho_G}{\rho_L}\left(1 - x_e\right)\right) \qquad [18.5.14]$$

For values of x_e greater than unity (i.e. when the enthalpy added to the fluid places its equilibrium state in the superheated vapor region), x_e is set equal to 1.0 in the above expression. The difference between the actual vapor enthalpy $h_{G,a}$ and the equilibrium vapor enthalpy $h_{G,e}$ is given by

$$\frac{h_{G,a} - h_{G,e}}{h_{LG}} = \exp(-\tan \psi) \qquad [18.5.15]$$

The correlating parameter ψ is obtained with the following expression

$$\psi = a_1 Pr_G^{a_2} Re_{GH,e}^{a_3} \left(\frac{q d_i c_{pG,e}}{k_G h_{LG}}\right)^{a_4} \sum_{i=0}^{2} b_i x_e^i \qquad [18.5.16]$$

which is valid for $0 \le \psi \le \pi/2$. Furthermore, when $\psi < 0$, its value is set to 0.0; when $\psi > \pi/2$, it is set to $\pi/2$. The empirical values determined from a database of 1400 points for only water are as follows:

$a_1 = 0.13864$, $a_2 = 0.2031$, $a_3 = 0.20006$, $a_4 = -0.09232$
$b_0 = 1.3072$, $b_1 = -1.0833$, $b_2 = 0.8455$

For $0 \le x_e \le 1$, the equilibrium vapor enthalpy $h_{G,e}$ is that of the saturated vapor, i.e.

$$h_{G,e} = h_{G,sat} \qquad [18.5.17]$$

For $x_e > 1$, the equilibrium vapor enthalpy $h_{G,e}$ is calculated as

$$h_{G,e} = h_{G,sat} + (x_e - 1)h_{LG} \qquad [18.5.18]$$

This prediction method is implemented as follows to find the values of α, $T_{G,a}$ and x_a when given those of $\dot{m}$, x_e and q:

1. Estimate an initial value of $T_{G,f}$ to evaluate the fluid properties,
2. Use [18.5.14] and [18.5.16] to determine $Re_{GH,e}$ and ψ,
3. Utilize either [18.5.17] or [18.5.18] together with [18.5.15] to obtain $h_{G,a}$,
4. Input the value of $h_{G,a}$ into [18.5.12] to obtain x_a,
5. Solve [18.5.13] iteratively to find $T_{G,a}$,
6. Input the resulting values in [18.5.10] to determine the wall temperature T_w and then the heat transfer coefficient α,
7. A new film temperature $T_{G,f}$ may now be calculated with [18.5.11] and the whole procedure is repeated until the iteration reaches a stable result.

This method is more accurate than the simpler method of Groeneveld (1973) and has a similar range of application. The method does, however, ignore the effects of wall-to-droplet, vapor-to-droplet and radiation heat transfer, but importantly it does include the effect of departure from equilibrium.

18.5.4 Ganic and Rohsenow Method

Ganic and Rohsenow (1977) proposed a more complete model for heat transfer in the mist flow regime. The total heat flux was assumed to be the sum of three contributions: wall-to-vapor convection q_G, wall-to-droplet evaporation q_L and radiation q_r. Thus, the total heat flux is the sum of these contributions so that

$$q = q_G + q_L + q_r \qquad [18.5.19]$$

They predict the wall-to-vapor convection contribution using a modification of the McAdams turbulent flow correlation as follows

$$q_G = 0.0023 \left(\frac{k_G}{d_i} \right) \left(\frac{\dot{m}xd_i}{\varepsilon\mu_G} \right)^{0.8} Pr_G^{0.4} \left(T_w - T_{sat} \right) \qquad [18.5.20]$$

The Reynolds number includes the void fraction ε to determine the mean velocity of the vapor phase while the physical properties are evaluated at the saturation temperature. The total radiation contribution is the sum of the radiation from the wall-to-droplets and from the wall-to-vapor:

$$q_r = F_{wL}\sigma_{SB}\left(T_w^4 - T_{sat}^4\right) + F_{wG}\sigma_{SB}\left(T_w^4 - T_{sat}^4\right)$$

[18.5.21]

F_{wL} and F_{wG} are the respective view factors, σ_{SB} is the Stephan-Boltzmann constant ($\sigma_{SB} = 5.67 \times 10^{-8}$ W/m^{2}K^4) and blackbody radiation is assumed. For a transparent vapor, F_{wG} equals 0. Based on their subsequent simulations, the radiant heat flux is negligible except at very large wall temperatures.

The interesting aspect of this model is that a detailed analysis of the wall-to-droplet heat transfer mechanisms was attempted, although non-equilibrium effects were ignored. They proposed the following expression for the heat flux due to this impinging droplet mechanism:

$$q_L = u_d\left(1-\varepsilon\right)\rho_L h_{LG} f_{cd} \exp\left[1 - \left(\frac{T_w}{T_{sat}}\right)^2\right]$$

[18.5.22]

where the droplet deposition velocity u_d is calculated from

$$u_d = 0.15\frac{\dot{m}x}{\rho_L\varepsilon}\sqrt{\frac{f_G}{2}}$$

[18.5.23]

In the above expressions f_{cd} is the cumulative deposition factor and f_G is the single-phase friction factor calculated at the effective vapor Reynolds number, i.e. ($\dot{m}x_e d_i)/(\varepsilon\mu_G)$. A complex method was presented for determination of f_{cd} as a function of droplet size and can be found in the original reference. Because of the larger quantity of liquid at lower vapor qualities, there is a higher propensity for the liquid to contact the hot tube wall at these conditions. Hence the importance of q_L to heat transfer is more significant at low to medium vapor qualities than at high vapor qualities, where non-equilibrium effects become important.

18.6 Critical Heat Flux in Vertical Channels

The critical heat flux in tubes and channels has been investigated extensively and the reader is referred to Chapters 8 and 9 in Collier and Thome (1994) for an extensive review of prediction methods and parameters influencing the process. Presently, the critical heat flux occurring in uniformly heated vertical tubes is addressed and the widely quoted, general method of Katto and Ohno (1984) is presented below. This method is the result of progressive improvements over the years and is applicable to a wide range of conditions for which the critical heat flux is reached in the saturated zone of a vertical tube for saturated or subcooled liquid inlet conditions. In their method, the critical heat flux q_{crit} is determined from the following expression that corrects for the level of inlet subcooling as follows:

$$q_{crit} = q_{crit,i}\left[1 + K_i\left(\frac{\Delta h_{L,inlet}}{h_{LG}}\right)\right]$$

[18.6.1]

where $q_{crit,i}$ is a reference critical heat flux at saturated liquid inlet conditions obtained from one of five different correlations to be given below, K_i is an inlet subcooling factor and $h_{L,inlet}$ is the change of enthalpy of the liquid from its subcooled inlet temperature to its saturation temperature. Their method uses the following three dimensionless groups:

$$Z = z/d_i \qquad [18.6.2]$$

$$R = \rho_G/\rho_L \qquad [18.6.3]$$

$$W = \frac{\sigma\rho_L}{\dot{m}^2 z} \qquad [18.6.4]$$

Depending on the operating conditions, there are five methods to choose from to determine the reference critical heat flux $q_{crit,i}$ as follows:

$$\frac{q_{crit,1}}{\dot{m}h_{LG}} = \frac{CW^{0.043}}{Z} \qquad [18.6.5]$$

$$\frac{q_{crit,2}}{\dot{m}h_{LG}} = \frac{0.1\,R^{0.133}W^{0.333}}{1+0.0031\,Z} \qquad [18.6.6]$$

$$\frac{q_{crit,3}}{\dot{m}h_{LG}} = \frac{0.098\,R^{0.133}W^{0.433}Z^{0.27}}{1+0.0031\,Z} \qquad [18.6.7]$$

$$\frac{q_{crit,4}}{\dot{m}h_{LG}} = \frac{0.0384\,R^{0.6}W^{0.173}}{1+0.28\,W^{0.233}Z} \qquad [18.6.8]$$

$$\frac{q_{crit,5}}{\dot{m}h_{LG}} = \frac{0.234\,R^{0.513}W^{0.433}Z^{0.27}}{1+0.0013\,Z} \qquad [18.6.9]$$

The value of K_i in [18.6.1] also depends on the particular conditions and is determined with one of the following three expressions:

$$K_1 = \frac{0.261}{CW^{0.043}} \qquad [18.6.10]$$

$$K_2 = \frac{0.833[0.0124+(1/Z)]}{R^{0.133}W^{0.333}} \qquad [18.6.11]$$

$$K_2 = \frac{1.12[1.52W^{0.233}+(1/Z)]}{R^{0.6}W^{0.173}} \qquad [18.6.12]$$

The value of C is given by:

C = 0.25 for Z < 50
C = 0.25+0.0009(Z-50) for $50 \le Z \le 150$

C = 0.34 for Z > 50.

The appropriate choice of expressions to use for $q_{crit,i}$ and K_i is determined as follows:

<u>For R < 0.15</u>:

if $q_{crit,1} < q_{crit,2}$,	then $q_{crit,i} = q_{crit,1}$;
if $q_{crit,1} > q_{crit,2}$ and $q_{crit,2} < q_{crit,3}$,	then $q_{crit,i} = q_{crit,2}$;
if $q_{crit,1} > q_{crit,2}$ and $q_{crit,2} > q_{crit,3}$,	then $q_{crit,i} = q_{crit,3}$;
if $K_1 > K_2$,	then $K_i = K_1$;
if $K_1 < K_2$,	then $K_i = K_2$.

<u>For R > 0.15</u>:

if $q_{crit,1} < q_{crit,5}$,	then $q_{crit,i} = q_{crit,1}$;
if $q_{crit,1} > q_{crit,5}$ and $q_{crit,5} > q_{crit,4}$,	then $q_{crit,i} = q_{crit,5}$;
if $q_{crit,1} > q_{crit,5}$ and $q_{crit,5} < q_{crit,4}$,	then $q_{crit,i} = q_{crit,4}$;
if $K_1 > K_2$,	then $K_i = K_1$;
if $K_1 < K_2$ and $K_2 < K_3$,	then $K_i = K_2$;
if $K_1 < K_2$ and $K_2 > K_3$,	then $K_i = K_3$.

Their critical heat flux database covers the following conditions:

$0.01 < z < 8.8$ m
$0.001 < d_i < 0.038$ m
$5 < Z < 880$
$0.0003 < R < 0.41$
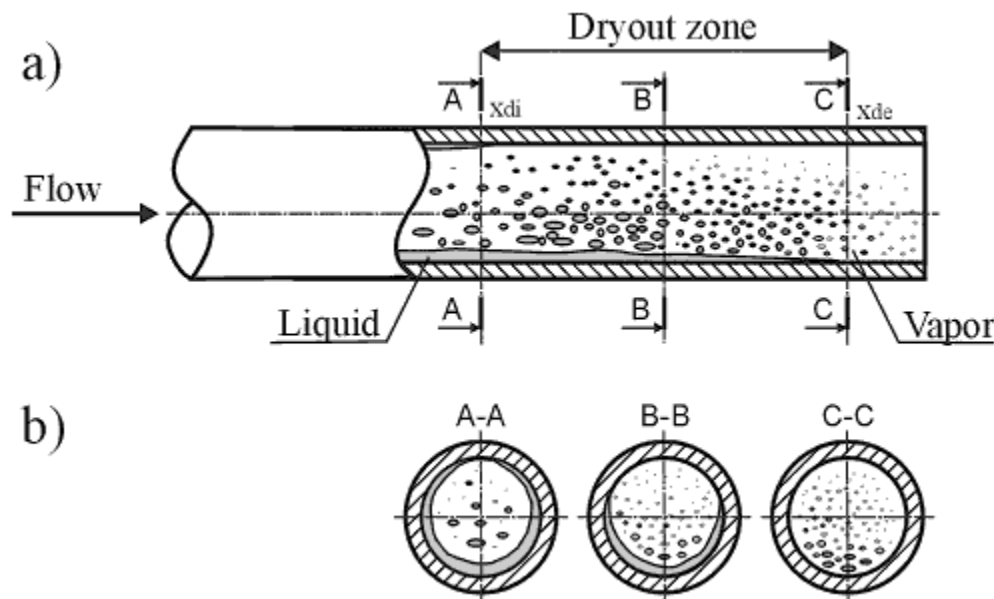$3 \times 10^{-9} < W < 0.02$
$0.4 < \Delta h_{LG} < 39.9$ kJ/kg

Furthermore, mass velocities in their database ranged from about 11-8800 kg/m^{2}s while the test fluids were refrigerants (R-12, R-22, R-115) and liquid helium. The critical heat flux condition is normally reached at or near the exit of the tube. The exit vapor quality x_{exit} corresponding to q_{crit} can be obtained from an energy balance along the tube from its inlet, so that:

$$x_{exit} = \frac{4q_{crit}}{\dot{m}h_{LG}}\left(\frac{z}{d_i}\right) - \frac{\Delta h_{L,inlet}}{h_{LG}}$$

[18.6.13]

18.7 Heat Transfer with Progressive Dryout in Horizontal Tubes

The process of evaporation in *horizontal tubes* during the transition from annular flow to mist flow is depicted in Figure 18.4. Dryout occurs first at the top of the tube where the liquid film is thinner, denoted as vapor quality x_{di} (section A-A), and then progresses downward around the perimeter (section B-B) until reaching the bottom (section C-C) at the vapor quality x_{de}. The process of dryout thus takes place over a vapor quality range and ends at the bottom of the tube when the fully developed mist flow regime

is reached. This regime between x_{di} and x_{de} will be called dryout (in contrast, dryout in a vertical tube is typically assumed to occur simultaneously around the entire perimeter of the tube at one particular vapor quality). The mist flow heat transfer methods described above, when applied to horizontal tubes, do *not* account for this progressive transition from annular to mist flow and hence cannot predict the heat transfer coefficient in the dryout regime.

Figure 18.4. (a) Dryout zone during evaporation in a horizontal tube; (b) Cross sectional views: A-A onset of dryout in annular flow at top of tube; B-B partial dryout around tube perimeter; C-C end of dryout at bottom of tube and beginning of mist flow.

The onset of dryout at the top of a horizontal tube is accompanied by a drastic drop in the heat transfer coefficient relative to that prior to dryout (annular flow typically). The heat transfer coefficient falls rapidly in the dryout zone as a smaller and smaller fraction of the tube perimeter is wetted by what is left of the annular liquid film and then becomes nearly constant in value when the mist flow regime is reached, as seen in Figure 18.5 of Mori et al. (2000) while noting that the lines AB, BC and CD represent a fit to the data points, not a prediction method. The point of intersection B indicates the inception point of dryout at the top of the horizontal tube, where locally the heat transfer begins to fall as the annular film dries out. The point of intersection C indicates the location where dryout is complete around the tube perimeter, and thus also where the deterioration of heat transfer ends. The dryout qualities at inception and ending of this process at these respective points are denoted x_{di} and x_{de}. The distinction of these two points is caused by the shift of the dryout position from the top to the bottom around and along the tube perimeter with increasing quality. The heat transfer process from point A to B is that of annular flow boiling while that from C to D is mist flow heat transfer. From B to C, a transition zone exists that will be called ***dryout heat transfer*** here to distinguish it from ***mist flow heat transfer***.
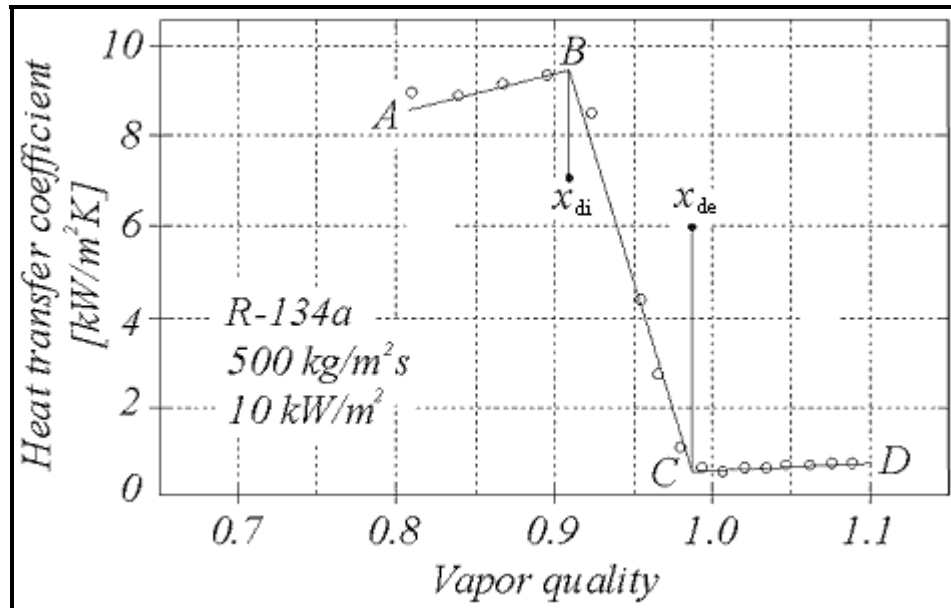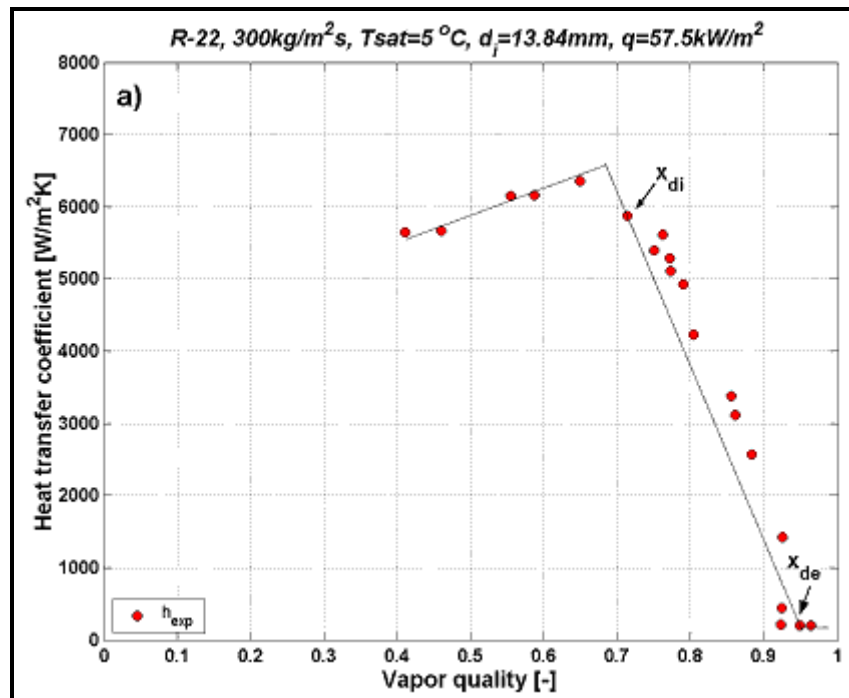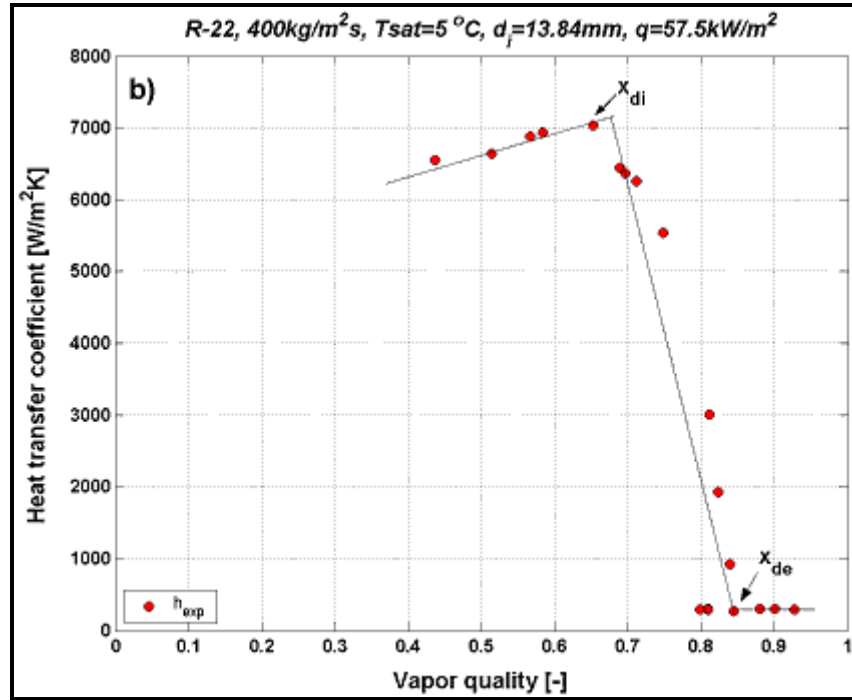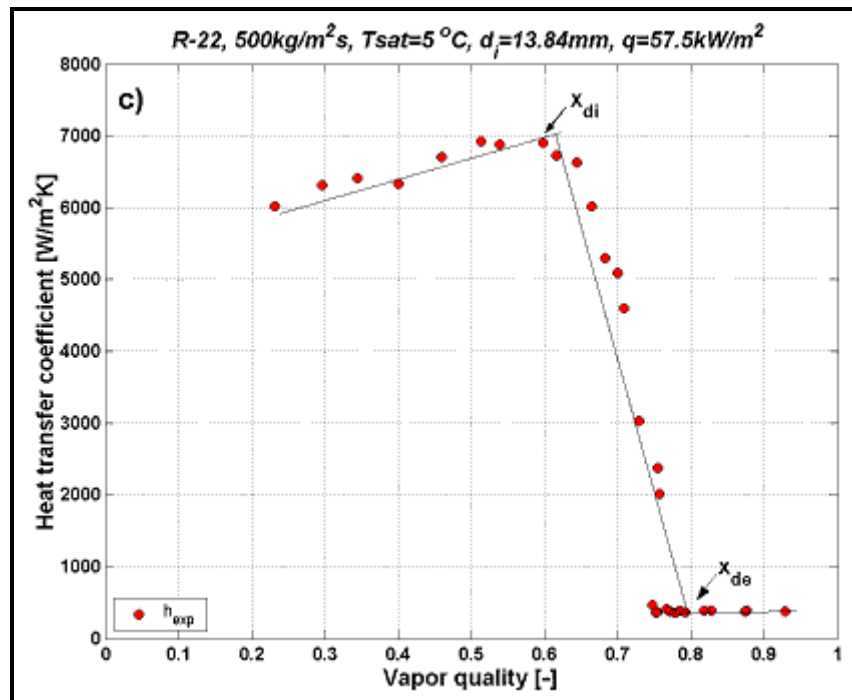
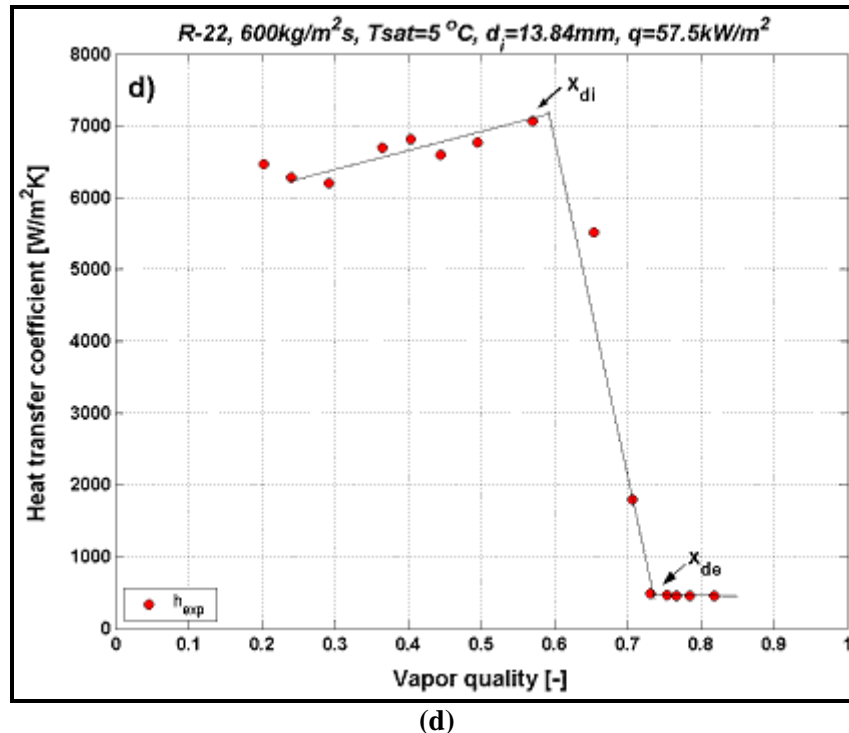**Figure 18.5. Variation in local heat transfer coefficient during dryout from Mori et al. (2000).**
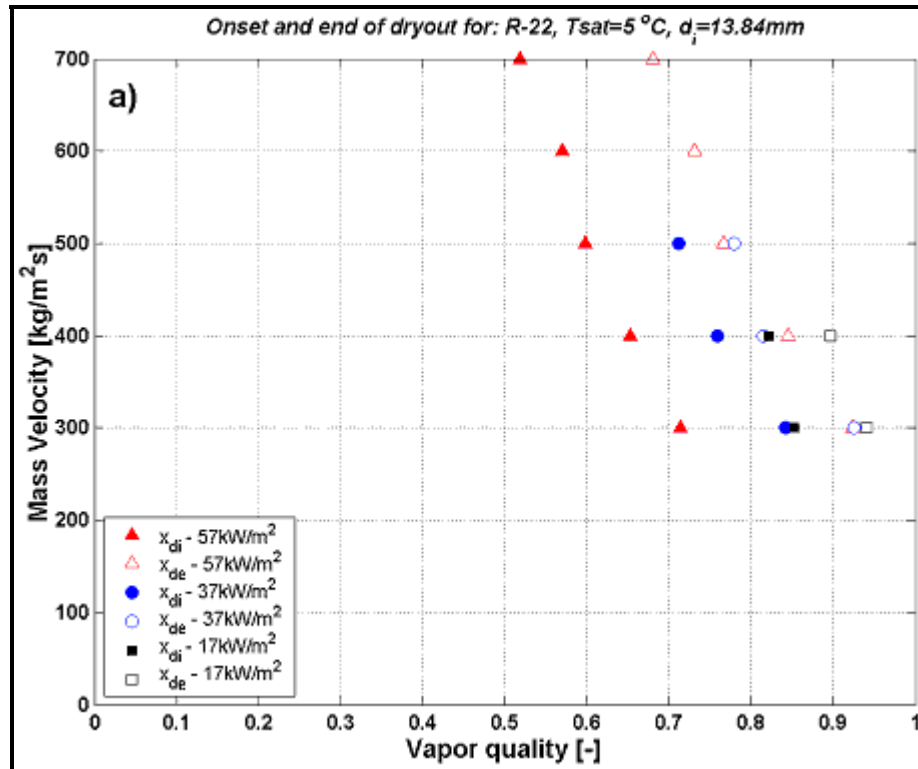

(a)

(b)

(c)

(d)
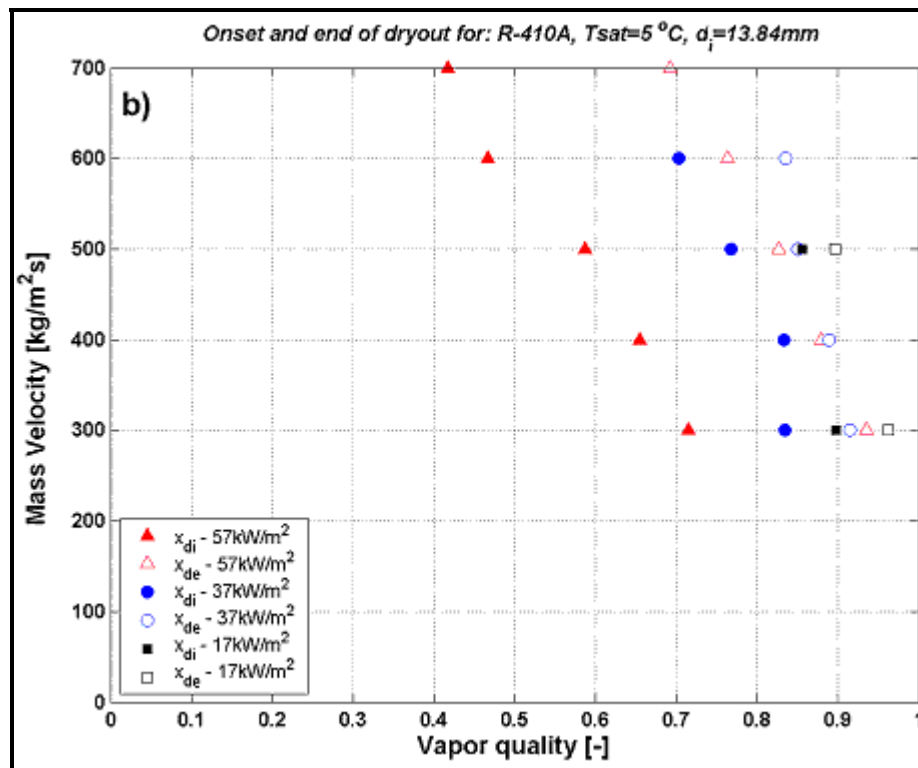
Figure 18.6. Heat transfer for R-22 with an initial heat flux $q = 57.5$
kW/m^2 before the onset of dryout at four mass velocities: a) 300
kg/m^{2}s, b) 400 kg/m^{2}s, c) 500 kg/m^{2}s; d) 600 kg/m^{2}s.

Figure 18.6 shows similar results for the transition from annular flow to mist flow in tests done by Wojtan, Ursenbacher and Thome (2005a) for evaporation of R-22 in a horizontal 13.84 mm internal diameter, plain copper tube at 5°C using hot water heating (again with the lines through the data indicating trends, not prediction methods). The exact vapor quality at the onset of dryout x_{di} is not known because of the finite number of tests run and hence its expected point of occurrence is indicated. The end of dryout is also indicated by x_{de}. Some hysteretic effect was also noted when going back into the dryout zone from mist flow but this complication was for now ignored. They did systematic tests for onset heat fluxes ranging from 7.5 to 57.5 kW/m^2 for R-22 and R-410A in 8.00 and 13.84 mm internal diameter tubes in order to develop a database on the effect of heat flux on the dryout process. Analyzing all their series of test results, the dryout inception vapor qualities x_{di} and dryout ending vapor qualities x_{de} were found from their R-22 and R-410A data and are presented in Figure 18.7 for two tube diameters as a function of heat flux. Comparing the dryout inception points for both fluids, it can be seen that x_{di} occurs earlier for R-410A than for R-22. This can be explained by the influence of surface tension, which is 30% lower for R-410A than R-22. That is, as the surface tension decreases, the vapor shear meets less resistance to entrain the liquid film into the high velocity vapor core and thus the inception of dryout is therefore encountered at a lower vapor quality for R-410A compared to that for R-22.
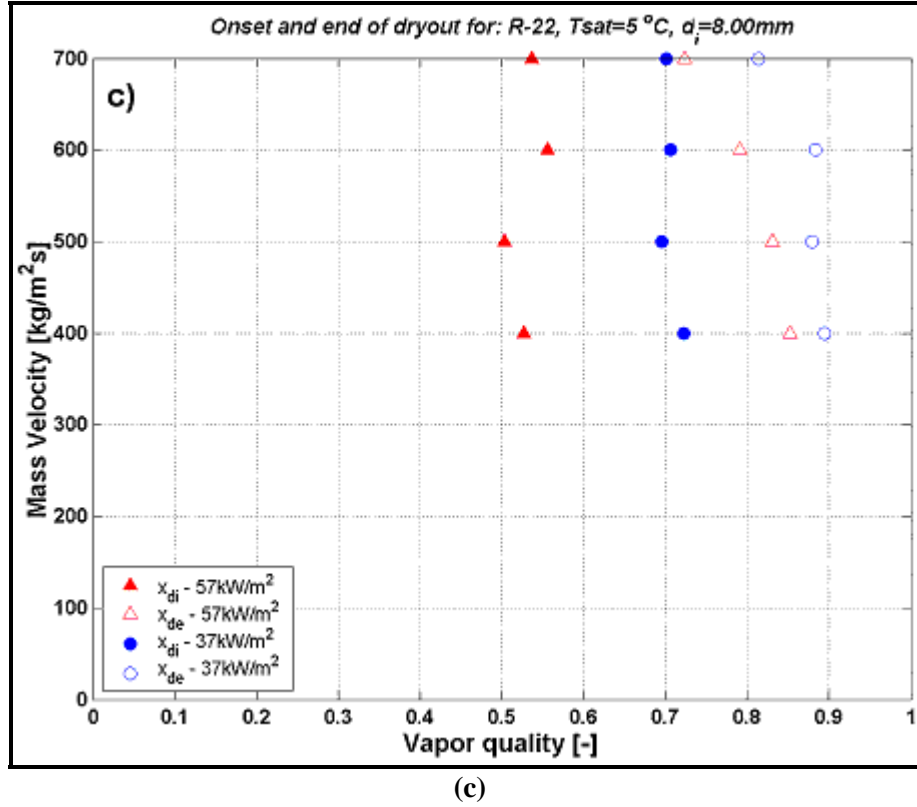
(a)

(b)

(c)

Figure 18.7. The dryout inception x_{di} and the dryout completion x_{de} for: (a) R-22, d_i = 13.84 mm; (b) R-410A, d_i = 13.84 mm; (c) R-22, d_i = 8.00 mm from Wojtan, Ursenbacher and Thome (2005a).

Mori et al. (2000) classified their dryout results into three characteristic regimes (S1, S2 and S3) based on the experimental trends they observed and presented prediction methods for their values of x_{di} and x_{de}. The Wojtan, Ursenbacher and Thome (2005a) experimental data agreed best, qualitatively speaking, with the dryout regime S2 prediction method where the inception x_{di} and dryout completion x_{de} expressions are as follows:

$$x_{di} = 0.58 \exp\left[0.52 - 0.000021 We_G^{0.96} Fr_G^{-0.02} \left(\frac{\rho_G}{\rho_L} \right)^{-0.08} \right] \qquad [18.7.1]$$

$$x_{de} = 0.61 \exp\left[0.57 - 0.0000265 We_G^{0.94} Fr_G^{-0.02} \left(\frac{\rho_G}{\rho_L} \right)^{-0.08} \right] \qquad [18.7.2]$$

In these expressions, the Weber and Froude numbers are defined as:

$$We_G = \frac{\dot{m}^2 d_i}{\rho_G \sigma} \qquad [18.7.3]$$

$$Fr_G = \frac{\dot{m}^2}{\rho_G (\rho_L - \rho_G) g d_i} \qquad [18.7.4]$$

The above approach has been extended by Wojtan, Ursenbacher and Thome (2005a) to include the strong influence of heat flux they observed. This was incorporated by introducing a non-dimensional heat flux term in the above expressions and then finding new empirical constants using their heat flux dependent database. Thus, the new criteria for the beginning and ending of dryout are calculated from their following equations, where q is the heat flux just prior to the onset of dryout:

$$x_{di} = 0.58 \exp\left[0.52 - 0.235 \text{We}_G^{0.17} \text{Fr}_G^{0.37} \left(\frac{\rho_G}{\rho_L}\right)^{0.25} \left(\frac{q}{q_{DNB}}\right)^{0.70}\right] \qquad [18.7.5]$$

$$x_{de} = 0.61 \exp\left[0.57 - 0.0058 \text{We}_G^{0.38} \text{Fr}_G^{0.15} \left(\frac{\rho_G}{\rho_L}\right)^{-0.09} \left(\frac{q}{q_{DNB}}\right)^{0.27}\right] \qquad [18.7.6]$$

Applying these expressions, an additional rule is that $x_{de} = x_{di}$ when [18.7.6] gives a smaller value than that given by [18.7.5], i.e. no cross over of these transition lines is allowed. Also, the maximum value in applying the method is $x_{de} = 0.99$, i.e. $x_{de} = 0.99$ whenever $x > 0.99$. The definitions of We_G and Fr_G remain the same as above and the heat flux at departure from nucleate boiling q_{DNB} is that of Kutateladze (1948):

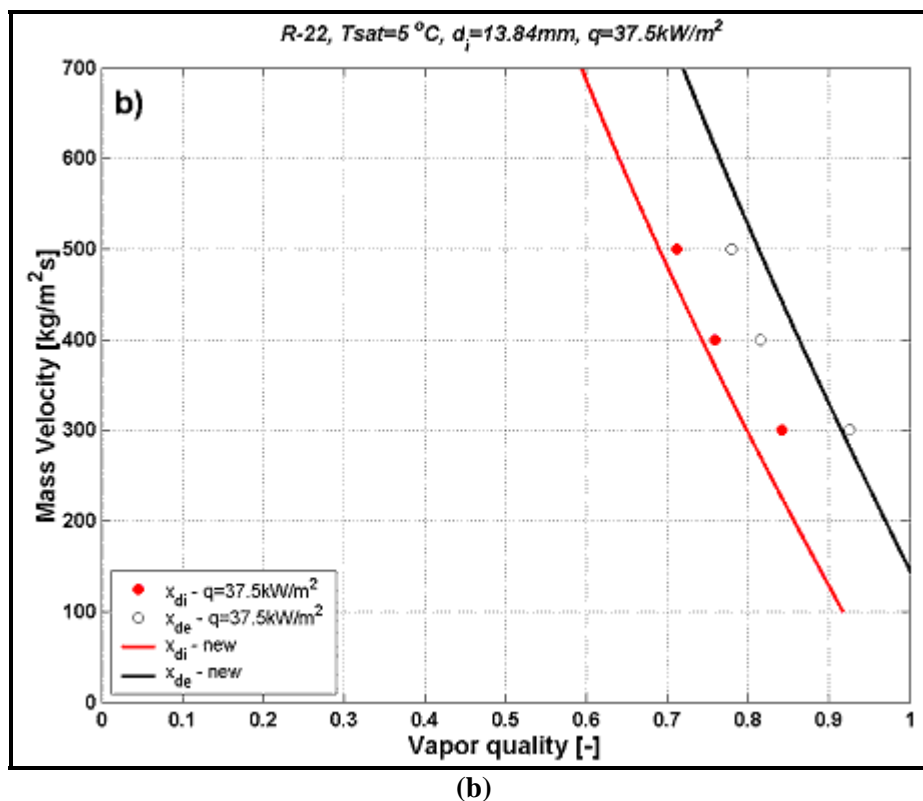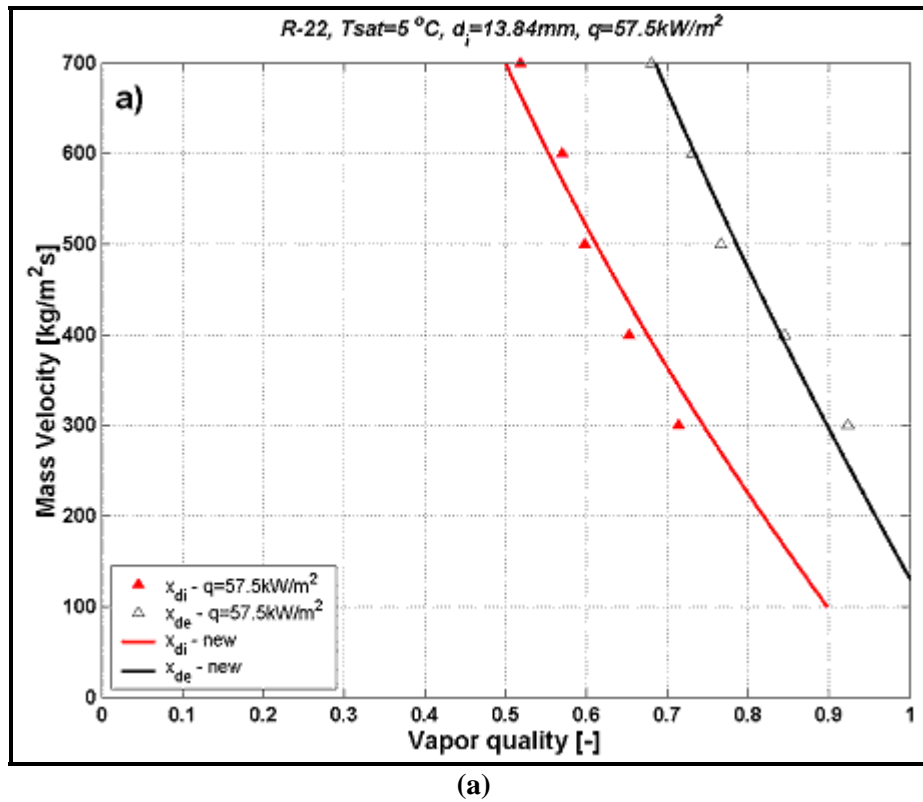$$q_{DNB} = 0.131 \rho_G^{0.5} h_{LG} \left(g(\rho_L - \rho_G)\sigma\right)^{0.25} \qquad [18.7.7]$$

Important from an application point-of-view, besides determining the respective values of x_{di} and x_{de}, the above expressions can be inverted to obtain the transition mass velocities for the initiation and ending of the dryout zone, respectively, as a function of vapor quality:
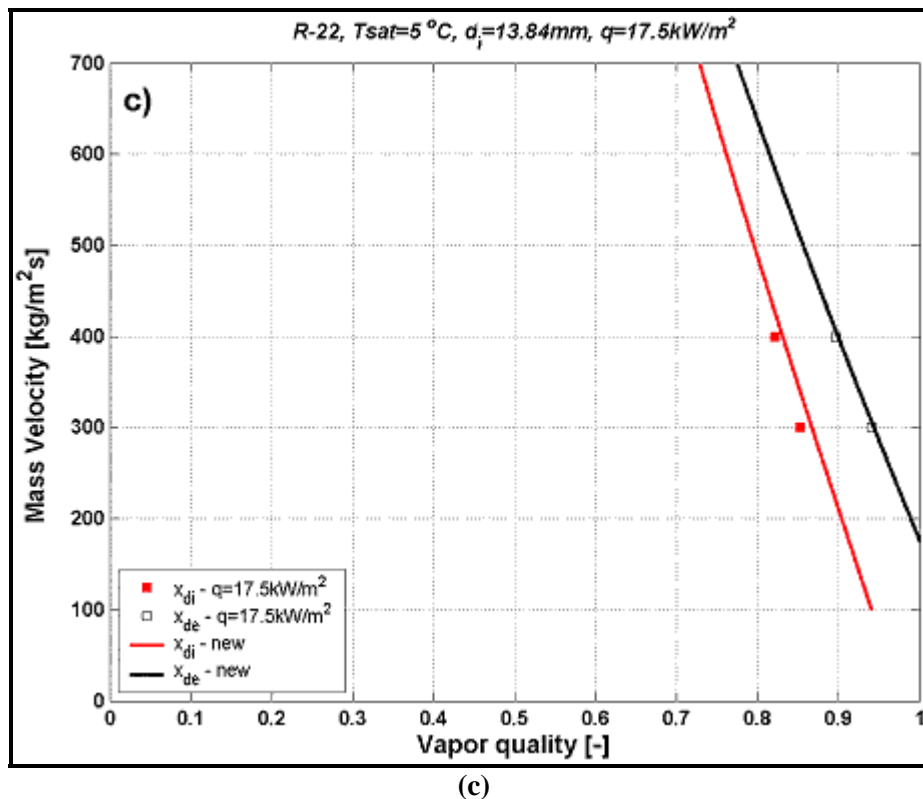
$$\dot{m}_{dryout} = \left[\frac{1}{0.235}\left(\ln\left(\frac{0.58}{x}\right) + 0.52\right)\left(\frac{d_i}{\rho_G \sigma}\right)^{-0.17}\left(\frac{1}{g d_i \rho_G (\rho_L - \rho_G)}\right)^{-0.37}\left(\frac{\rho_G}{\rho_L}\right)^{-0.25}\left(\frac{q}{q_{DNB}}\right)^{-0.70}\right]^{0.926}$$

$$[18.7.8]$$

$$\dot{m}_{mist} = \left[\frac{1}{0.0058}\left(\ln\left(\frac{0.61}{x}\right) + 0.57\right)\left(\frac{d_i}{\rho_G \sigma}\right)^{-0.38}\left(\frac{1}{g d_i \rho_G (\rho_L - \rho_G)}\right)^{-0.15}\left(\frac{\rho_G}{\rho_L}\right)^{0.09}\left(\frac{q}{q_{DNB}}\right)^{-0.27}\right]^{0.943}$$

$$[18.7.9]$$

Figure 18.8 illustrates the new transition curves calculated from the new expressions compared to the values of x_{di} and x_{de} obtained during their evaporation tests with R-22 in a 13.84 mm internal diameter test section. As can be seen, very good agreement has been found for all three initial heat fluxes. Similar results were obtained for the evaporation tests with R-410A and for their 8.0 mm tube. It should be noted that the above dryout criteria were developed from tests with hot water heated tubes; many tests in the literature use direct Joule heating of the tube and hence the dry fraction of the perimeter experiences an uncharacteristically large rise in wall temperature which tends to propagate around and up the tube,

rendering such results less useful for development of thermal design methods in and near the dryout regime.

(a)

(b)

(c)

Figure 18.8. New annular-to-dryout and dryout-to-mist flow transition expressions compared experimental results of R-22 in the 13.84 mm test section at three initial heat fluxes: (a) 57.5 kW/m^2, (b) 37.5 kW/m^2, (c) 17.5 kW/m^2.

Defining mist flow heat transfer coefficients as those results when $x > x_{de}$, Wojtan, Ursenbacher and Thome (2005b) noted that the mist flow heat transfer coefficients increased with increasing mass velocity but did not show any significant influence from the initial heat flux that was responsible for the onset of dryout. Furthermore, the measured vapor temperatures in the mist flow regime also corresponded to those calculated at the exit saturation pressure, which means that no vapor superheating or departure from equilibrium was observed at the current mist flow test conditions. Since using hot water heating precludes a significant increase in the wall temperature compared to those with imposed heat fluxes (electrically heated test sections), a notable departure from equilibrium is not expected. The flow pattern oriented, flow boiling model of Kattan, Thome and Favrat (1998a, 1998b, 1998c), presented elsewhere in Chapter 10, does not cover either the new dryout or the mist flow heat transfer regimes. Thus, the new methods proposed by Wojtan, Ursenbacher and Thome (2005b) to cover both the mist flow regime and the dryout regime are presented below.

Since vapor and liquid phases were observed to be in thermal equilibrium during evaporation in mist flow during the above Wojtan-Ursenbacher-Thome tests, the measured heat transfer coefficients were compared to the thermal equilibrium correlations of Dougall and Rohsenow (1963) and Groeneveld (1973) presented earlier. The Dougall-Rohsenow method was found to significantly over predict their R-22 and R-410A data while that of Groeneveld gave more reasonable results, over predicting by an average of 13.6%, which is quite good when considering that their method was extrapolated beyond its original range to much lower heat fluxes, pressures and mass velocities (as documented earlier, the database Groeneveld used to determine his empirical factors covered high mass velocities, saturation pressures and

heat fluxes, mostly for water). Based on the new R-22 and R-410A mist heat transfer data, the correlation of Groeneveld was re-optimized for the prediction of the mist flow heat transfer coefficients at design conditions typical of direct-expansion evaporators for refrigerants. Hence, for tube diameters from 8.00 to 13.84 mm and mass velocities from 300-700 kg/m²s, Wojtan, Ursenbacher and Thome (2005b) made a modified Groeneveld correlation where equation [18.5.8] has been changed as below to calculate the mist heat transfer coefficient when $x \geq x_{de}$:
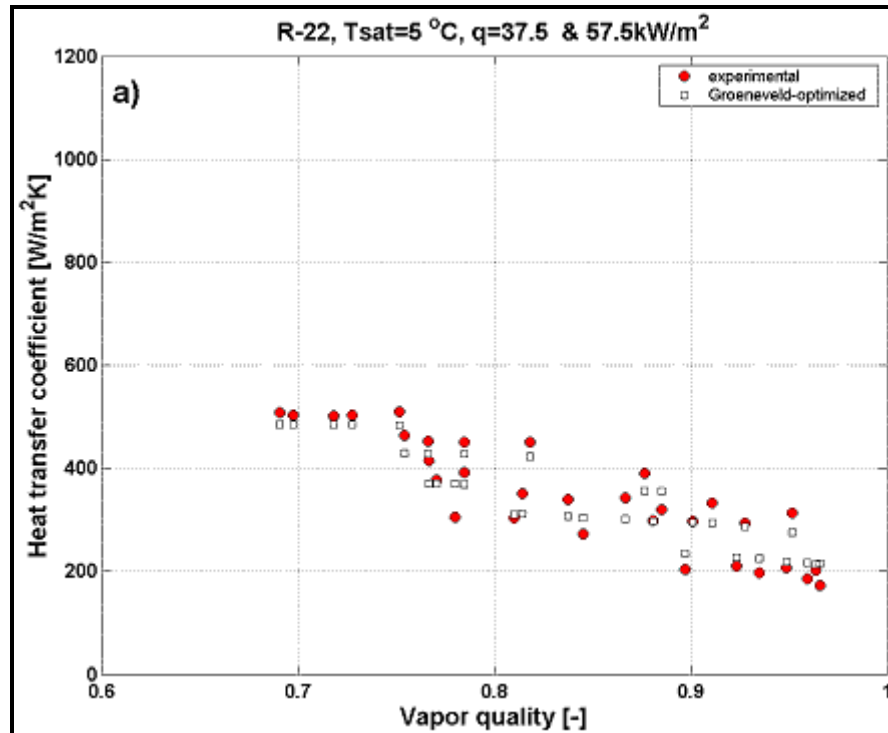
$$\text{Nu}_G = \frac{\alpha d_i}{k_G} = 0.0117 \left\{ \frac{\dot{m} d_i}{\mu_G} \left[x + \frac{\rho_G}{\rho_L}(1-x) \right] \right\}^{0.79} \text{Pr}_G^{1.06} \, Y^{-1.83} \qquad [18.7.10]$$

The definition of Y remains the same as before in [18.5.7]. Compared to the original version, the values of exponents and leading constant were changed and the new exponent on the Reynolds number (0.79) becomes nearly that of a single phase flow (0.80). Figure 18.9 shows the comparison of the mist flow heat transfer results measured in the 13.84 mm test section with the new method for both refrigerants. The agreement of the experimental and predicted points was improved and statistical analysis gave an average deviation, mean deviation and standard deviation for all 71 experimental points of only -0.04%, 6.31% and 8.32% using the new modified version, respectively. The new method predicts 93% of experimental results obtained for the two refrigerants at five different mass velocities and two different initial heat fluxes within ±15% error.
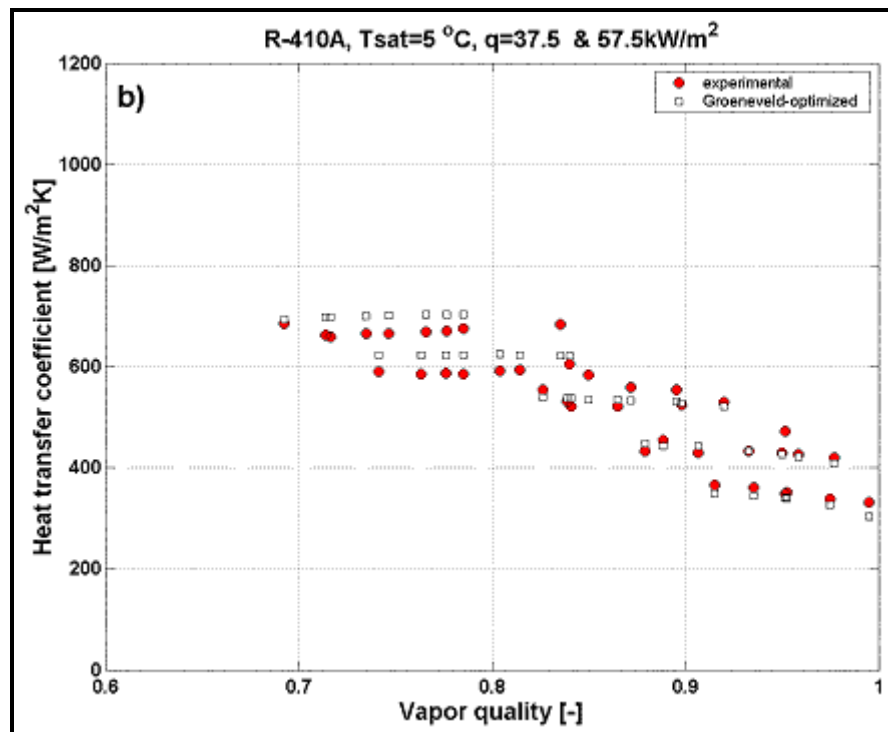
As has been shown earlier, the heat transfer coefficient falls sharply in the dryout region until it reaches mist flow. For the dryout region in the range $x_{di} > x > x_{de}$, the dryout heat transfer coefficient α_{dryout} at a particular vapor quality x is calculated from the following linear interpolation:

$$\alpha_{dryout} = \alpha_{tp}(x_{di}) - \frac{x - x_{di}}{x_{de} - x_{di}} \left[\alpha_{tp}(x_{di}) - \alpha_{mist}(x_{de}) \right] \qquad [18.7.11]$$

In this expression, $\alpha_{tp}(x_{di})$ is the two-phase flow heat transfer coefficient prior to dryout inception at x_{di} evaluated at its local pre-dryout heat flux and $\alpha_{mist}(x_{de})$ is the mist flow heat transfer coefficient calculated from [18.7.10] at the dryout completion quality x_{de}. The Kattan-Thome-Favrat method for calculating α_{tp} at x_{di} is described in Chapter 10. This interpolation approach works fairly well (considering the sharp fall in the dryout heat transfer coefficient with vapor quality that unavoidably creates sizable errors in α_{dryout} with only small errors in x) and smoothly links the heat transfer coefficients in the annular and mist flow regimes. This simple linear interpolation method has a tendency to under predict heat transfer coefficients in the dryout region. Furthermore, it should be noted that the dryout regime and its heat transfer coefficients are particularly sensitive to the predicted values of x_{di} and x_{de} and that the above methods are derived only for a limited range of test conditions (R-22 and R-410A at 5°C). The Kattan-Thome-Favrat flow pattern based flow boiling heat transfer model has thus now been extended to all flow patterns except bubbly flow, which occurs at very high mass velocities outside of normal engineering practice.

(a)

(b)

Figure 18.9. Comparison of the mist flow heat transfer results measured in the 13.84 mm test section with the new version of Groeneveld correlation for: (a) R-22, (b) R-410A.

Example 18.3: Determine the vapor qualities at the initiation and ending of dryout in an 8.0 mm tube evaporating R-134a at 4°C (3.377 bar) for a mass velocity of 300 kg/m²s where the local heat flux prior to the initiation of dryout is 15 kW/m².

Solution: The properties required are:

$\rho_L = 1281$ kg/m³; $\rho_G = 16.56$ kg/m³; $h_{LG} = 195500$ J/kg; $\sigma = 0.011$ N/m.

Weber and Froude numbers are determined from [18.7.3] and [18.7.4]:

$$We_G = \frac{\dot{m}^2 d_i}{\rho_G \sigma} = \frac{300^2(0.008)}{16.56(0.011)} = 3952.6$$

$$Fr_G = \frac{\dot{m}^2}{\rho_G(\rho_L - \rho_G)gd_i} = \frac{300^2}{16.56(1281-16.56)(9.81)(0.008)} = 54.77$$

The heat flux at the departure from nucleate boiling is obtained from [18.7.7]:

$$q_{DNB} = 0.131\rho_G^{0.5}h_{LG}\left(g(\rho_L - \rho_G)\sigma\right)^{0.25}$$
$$= 0.131(16.56)^{0.5}(195500)(9.81(1281-16.56)0.011)^{0.25} = 356195 \text{ W/m}^2$$

The vapor qualities at the beginning and ending of dryout are calculated from [18.7.5] and [18.7.6]:

$$x_{di} = 0.58\exp\left[0.52 - 0.235We_G^{0.17}Fr_G^{0.37}\left(\frac{\rho_G}{\rho_L}\right)^{0.25}\left(\frac{q}{q_{DNB}}\right)^{0.70}\right]$$

$$= 0.58\exp\left[0.52 - 0.235(3952.6)^{0.17}(54.77)^{0.37}\left(\frac{16.56}{1281}\right)^{0.25}\left(\frac{15000}{356195}\right)^{0.70}\right]$$

$$= 0.835$$

$$x_{de} = 0.61\exp\left[0.57 - 0.0058We_G^{0.38}Fr_G^{0.15}\left(\frac{\rho_G}{\rho_L}\right)^{-0.09}\left(\frac{q}{q_{DNB}}\right)^{0.27}\right]$$

$$= 0.61\exp\left[0.57 - 0.0058(3952.6)^{0.38}(54.77)^{0.15}\left(\frac{16.56}{1281}\right)^{-0.09}\left(\frac{15000}{356195}\right)^{0.27}\right]$$

$$= 0.924$$

Thus, the annular flow heat transfer coefficient will begin to fall off sharply at $x_{di} = 0.835$ and will reach the mist flow heat transfer coefficient at $x_{de} = 0.924$; therefore, the dryout zone extends over a vapor quality change of about 0.09. If the inlet vapor quality to the direct-expansion evaporator after the expansion valve is assumed to be 0.28, then about 1/8th of the heat transfer occurs in the dryout regime and about 1/9th in the mist flow regime, both of which have a significant effect on the size of the resulting unit.

18.8 Droplet Heat Transfer

Besides convective heat transfer from the wall to the vapor, radiation from the wall to the droplets and radiation from the wall to the vapor and transient conduction from the wall to impinging droplets, the fourth heat transfer mechanism is evaporation of the entrained droplets by the superheated vapor. In this section, a simple analysis of heat transfer from the superheated vapor to an entrained liquid droplet will be presented.

For the simplified situation considered below by Ganic and Rohsenow (1977), heat transfer to a droplet is simulated utilizing methods developed for particulate flows. For a single particle, or, in this case, an isolated droplet, the droplet heat transfer coefficient α_D is estimated with the expression

$$\mathrm{Nu}_D = 2 + 0.6\,\mathrm{Re}_D^{1/2}\,\mathrm{Pr}_G^{1/3} \qquad [18.8.1]$$

The Nusselt number Nu_D in the above equation is defined based on the droplet diameter D. Similarly, the droplet Reynolds number Re_D is defined using the droplet diameter and the difference between the vapor velocity u_G and the droplet velocity u_D. These two dimensionless groups are given as

$$\mathrm{Nu}_D = \frac{\alpha_D D}{k_G} \qquad [18.8.2]$$

$$\mathrm{Re}_D = \frac{\rho_G D(u_G - u_D)}{\mu_G} \qquad [18.8.3]$$

The convective heat transfer coefficient from the vapor to the droplet is α_D and Prandtl number Pr_G is based on vapor properties as

$$\mathrm{Pr}_G = \frac{\mu_G c_{pG}}{k_G} \qquad [18.8.4]$$

In equation [18.8.1], the "2" on the right hand side is for pure conduction to the droplet while the second term accounts for convection to the droplet. The heat transfer to a droplet is driven by the temperature difference between the superheated vapor temperature $T_{G,a}$ and the droplet temperature T_D, the latter which is assumed to be the saturation temperature. The rate of heat transfer is given by

$$Q = \pi D^2 \alpha_D (T_G - T_D) \qquad [18.8.5]$$

One of the unknowns in the above analysis is the velocity difference, $(u_G - u_D)$. This difference may be obtained from a force balance on the droplet for vertical flow. If it is assumed that the droplet is spherical and not accelerating, then the hydrodynamic drag lifting the droplet is equal to the gravity force acting downward on it. The drag force F_{drag} is estimated from the drag coefficient as

$$C_{drag} = \frac{\left(\dfrac{F_{drag}}{\pi D^2/4}\right)}{\rho_G (u_G - u_D)^2 / 2} \qquad [18.8.6]$$

and the drag coefficient C_{drag} is calculated from

$$C_{drag} = \frac{24}{Re_D} + 0.44 \qquad [18.8.7]$$

The first term on the right hand side is the laminar flow term while the second is the turbulent term, such that the expression gives a reasonable representation of the drag over the whole range of Reynolds numbers. The gravity force acting on the droplet is

$$F_{drag} = \frac{\pi D^3}{6}(\rho_L - \rho_G)g \qquad [18.8.8]$$

and is thus a function of the droplet size. The initial droplet size is another important unknown. Whalley et al. (1982) suggest using the following equation

$$\frac{D}{d_i} = 1.9\, Re_G^{0.1}\, We_G^{-0.6}\left(\frac{\rho_G}{\rho_L}\right)^{0.6} \qquad [18.8.9]$$

In this expression the vapor phase Reynolds number Re_G for a tube with a diameter d_i is used:

$$Re_G = \frac{\dot{m}x d_i}{\mu_G} \qquad [18.8.10]$$

The vapor Weber number We_G of the tube is defined by Whalley et al. as:

$$We_G = \frac{\dot{m}^2 x^2 d_i}{\rho_G \sigma} \qquad [18.8.11]$$

As the liquid droplets evaporate and the vapor superheats, the value of u_G increases along the tube. Hence, the increased shear on the droplet interface may make the surface of the droplet become unstable. This instability is expected to occur when the droplet Weber number reaches a value of about 7.5 according to their analysis, where the droplet Weber number We_D is defined as

$$We_D = \frac{\rho_G(u_G - u_D)^2 D}{\sigma} \qquad [18.8.12]$$

At breakup of a droplet, it can be assumed that two new identical droplets are formed with a combined volume equal to that of the original droplet.

The rate of evaporation of a droplet Q is given by

$$\frac{dm}{dt} = \frac{Q}{h_{LG}} \qquad [18.8.13]$$

where m is the mass of the droplet. The mass of the droplet can be calculated from its diameter D and thus

$$m = \frac{1}{6} \pi D^3 \rho_L \qquad\qquad [18.8.14]$$

The rate of change of mass in the droplet is therefore given by

$$\frac{dm}{dt} = \frac{1}{2} \pi D^2 \rho_L \frac{dD}{dt} \qquad\qquad [18.8.15]$$

and it follows that

$$\frac{dD}{dt} = \frac{dm}{dt} \frac{2}{\pi D^2 \rho_L} \qquad\qquad [18.8.16]$$

The rate of change of the droplet diameter during its evaporation is thus

$$\frac{dD}{dt} = \frac{(2Q/h_{LG})}{\pi D^2 \rho_L} \qquad\qquad [18.8.17]$$

Utilizing a step-wise calculation approach for various droplet sizes up to their complete evaporation, the lifetimes of droplets can be estimated.

It can also be noted that as a droplet becomes small, the value of the droplet Reynolds number Re_D becomes small in [18.8.3]. Thus, the heat transfer is dominated by conduction from the vapor to the droplet interface and the heat transfer coefficient is inversely proportional to the droplet diameter D, i.e. $\alpha_D \propto 1/D$ in [18.8.1]. On the other hand, when the turbulence mode is dominant, the heat transfer coefficient is still inversely proportional to the droplet diameter but to the ½ power, i.e. $\alpha_D \propto 1/D^{1/2}$.

There are some aspects not addressed above. For instance, the non-equilibrium temperature of the vapor $T_{G,a}$ is another important unknown. The method presented earlier by Groeneveld and Delorme (1976) can be used to estimate its value. Just as important, the number of droplets and their size at any cross-section of the tube must be known in order to perform an energy balance along the heated flow channel. Consequently, modeling heat transfer in mist flow quickly becomes very complex. At the same time, the fundamental parameters that need to be measured experimentally to verify these methods are difficult to obtain without disturbing the flow itself.

Methods to numerically model the thermal hydrodynamics of mist flow have progressed rapidly in recent years. This is illustrated, for example, by the work of Andreani and Yadigaroglu (1997), who have developed a 3-dimensional Eulerian-Lagrangian model of dispersed flow boiling that includes a mechanistic description of the droplet spectrum evolution.

Homework Problems:

18.1: Determine the local mist flow heat transfer coefficient as a function of vapor quality at 0.5, 0.6, 0.7, 0.8 and 0.9 for a tube of 14 mm diameter and a flow rate of 0.1 kg/s. The fluid has the following physical properties: liquid density is 1147 kg/m^3, vapor density is 50 kg/m^3, vapor thermal conductivity is 0.011 W/mK, vapor specific heat of 1.7 kJ/kgK and vapor viscosity is 0.000012 Ns/m^2. Use the Dougall and Rohsenow method.

18.2: Repeat Problem 18.1 for an 8.0 mm diameter tube with a flow rate of 0.032653 kg/s.

18.3: Determine the local mist flow heat transfer coefficient for steam as a function of vapor quality at 0.5, 0.6, 0.7, 0.8 and 0.9 for a tube of 20 mm diameter and a flow rate of 0.3 kg/s. The steam /water system is at a saturation pressure of 40 bar with the following physical properties: liquid density is 1147 kg/m^3, vapor density is 50 kg/m^3, vapor thermal conductivity is 0.011 W/mK, vapor specific heat of 1.7 kJ/kgK and vapor viscosity is 0.000012 Ns/m^2. Use the Groeneveld method.

18.4: Repeat Example 18.3 for heat fluxes of 5, 10 and 20 kW/m^2 and comment on the trends observed.